Nano-Micro Letters

e-ISSN 2150-5551
CN 31-2103/TB

ARTICLE

https://doi.org/10.1007/s40820-023-01290-4

Cite as
Nano-Micro Lett.
(2024) 16:91

Received: 30 June 2023
Accepted: 16 November 2023

Moderate Fields, Maximum Potential: Achieving High Records with Temperature-Stable Energy Storage in Lead-Free BNT-Based Ceramics

Wenjing Shi[1], Leiyang Zhang[1], Ruiyi Jing[1], Yunyao Huang[1], Fukang Chen[2], Vladimir Shur[3], Xiaoyong Wei[1], Gang Liu[2] ✉, Hongliang Du[4] ✉, Li Jin[1] ✉

HIGHLIGHTS

- Achieving ultrahigh energy-storage density (7.19 J cm^{-3}) and outstanding storage efficiency (93.8%) at 460 kV cm^{-1} in BNT-based relaxor ferroelectric ceramics under a moderate electric field.
- Superior energy-storage performance accomplished through meticulous regulation of permittivity, enhancement of insulation quality, and strategic domain engineering via chemical formula optimization.
- The intricate structure–property relationship elucidated with precision using high-resolution transmission electron microscopy.

ABSTRACT The increasing awareness of environmental concerns has prompted a surge in the exploration of lead-free, high-power ceramic capacitors. Ongoing efforts to develop lead-free dielectric ceramics with exceptional energy-storage performance (ESP) have predominantly relied on multi-component composite strategies, often accomplished under ultrahigh electric fields. However, this approach poses challenges in insulation and system downsizing due to the necessary working voltage under such conditions. Despite extensive study, bulk ceramics of ($Bi_{0.5}Na_{0.5}$)TiO_3 (BNT), a prominent lead-free dielectric ceramic family, have seldom achieved a recoverable energy-storage (ES) density (W_{rec}) exceeding 7 J cm^{-3}. This study introduces a novel approach to attain ceramic capacitors with high ESP under moderate electric fields by regulating permittivity based on a linear dielectric model, enhancing insulation quality, and engineering domain structures through chemical formula

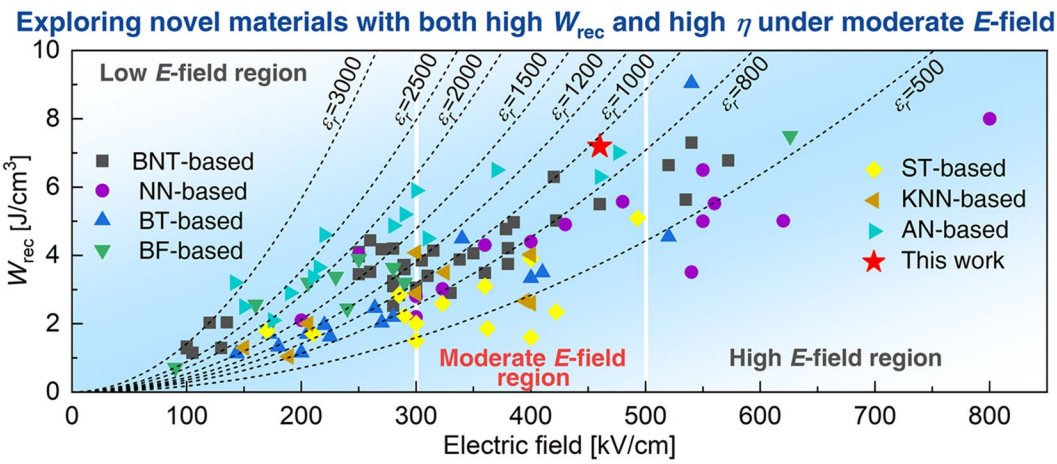

✉ Gang Liu, liugang13@swu.edu.cn; Hongliang Du, duhongliang@126.com; Li Jin, ljin@mail.xjtu.edu.cn
[1] Electronic Materials Research Laboratory, Key Laboratory of the Ministry of Education, School of Electronic Science and Engineering, Xi'an Jiaotong University, Xi'an 710049, People's Republic of China
[2] School of Materials and Energy, Southwest University, Chongqing 400715, People's Republic of China
[3] School of Natural Sciences and Mathematics, Ural Federal University, Ekaterinburg 620000, Russia
[4] Multifunctional Electronic Ceramics Laboratory, College of Engineering, Xi'an International University, Xi'an 710077, People's Republic of China

Published online: 18 January 2024

Shanghai Jiao Tong University Press

Springer

optimization. The incorporation of $SrTiO_3$ (ST) into the BNT matrix is revealed to reduce the dielectric constant, while the addition of $Bi(Mg_{2/3}Nb_{1/3})O_3$ (BMN) aids in maintaining polarization. Additionally, the study elucidates the methodology to achieve high ESP at moderate electric fields ranging from 300 to 500 kV cm^{-1}. In our optimized composition, $0.5(Bi_{0.5}Na_{0.4}K_{0.1})TiO_3$–0.5(2/3ST-1/3BMN) (B-0.5SB) ceramics, we achieved a W_{rec} of 7.19 J cm^{-3} with an efficiency of 93.8% at 460 kV cm^{-1}. Impressively, the B-0.5SB ceramics exhibit remarkable thermal stability between 30 and 140 °C under 365 kV cm^{-1}, maintaining a W_{rec} exceeding 5 J cm^{-3}. This study not only establishes the B-0.5SB ceramics as promising candidates for ES materials but also demonstrates the feasibility of optimizing ESP by modifying the dielectric constant under specific electric field conditions. Simultaneously, it provides valuable insights for the future design of ceramic capacitors with high ESP under constraints of limited electric field.

KEYWORDS BNT; Energy storage; Lead-free; Relaxor ferroelectrics; Capacitors

1 Introduction

In contrast with supercapacitors, lithium–ion batteries, and fuel cells, dielectric ceramic capacitors have emerged as a focal point in pulse electrical devices owing to their remarkable power density, rapid charge–discharge response, and broad operating temperature range [1–3]. However, their current bottleneck resides in a relatively lower energy-storage (ES) density, impeding widespread integration into pulse electrical devices [4–6]. Consequently, there is a pressing need to engineer dielectric materials with heightened energy-storage performance (ESP). The assessment of a dielectric material's ESP typically involves parameters such as W (total ES density), W_{rec} (recoverable ES density), W_{loss} (dissipated ES density), and η (ES efficiency). These parameters are determined through the measurement of polarization versus electric field (P–E) curves and are calculated using the following equations [7]:

$$W = \int_0^{P_{max}} E\,dP \tag{1}$$

$$W_{rec} = \int_{P_r}^{P_{max}} E\,dP \tag{2}$$

$$\eta = \frac{W_{rec}}{W}100\% = \frac{W_{rec}}{W_{rec} + W_{loss}}100\% \tag{3}$$

Here P_{max}, P_r, and E denote the maximum polarization, remnant polarization, and applied electric field (E-field), respectively. According to Eqs. (1–3), it is suggested that a dielectric material with a large ΔP ($= P_{max}–P_r$), high breakdown strength (BDS), and low P–E curve hysteresis would achieve high W_{rec} and η [8]. Dielectric materials are categorized into four types based on the characteristics of their P–E curves: linear dielectrics (LDs), normal ferroelectrics (FEs), antiferroelectrics (AFEs), and relaxor ferroelectrics (RFEs) [9]. LDs exhibit a linear relationship between E-field and induced polarization [10]. Despite this, their low P_{max} results in poor ESP. While FEs can achieve high P_{max}, the elevated P_r and substantial P–E hysteresis lead to poor P_r and η. Lead-containing AFEs, although possessing higher P_r, undergo an E-field-driven AFE-FE phase transition during electrical loading, resulting in lower η and a strain mutation at the critical E-field [11]. Consequently, RFEs outperform the other three types of dielectrics in terms of integrated ESP [12, 13].

The ESP of $(Bi_{0.5}Na_{0.5})TiO_3$ (BNT)-based bulk RFE ceramics has been extensively investigated in recent years [5, 6]. Figure 1a presents the W_{rec} of BNT-based ceramics plotted against the applied E-field, and Table S1 (refer to Supporting Information) summarizes the composition, maximum applied E-field (E_{max}), W_{rec}, and η for compared BNT-based bulk ceramics. In Fig. 1a, it is evident that W_{rec} generally increases with the applied E-field. Consequently, reducing permittivity (ε_r) and enhancing BDS emerge as effective strategies for enhancing the ESP of BNT-based ceramics. While efforts to reduce permittivity and improve BDS are relatively comparable, two critical challenges have been overlooked for an extended period. (1) Although increasing BDS enhances material ES capacity, working with strong E-fields poses challenges for miniaturization and integration. Operation at high fields (> 500 kV cm^{-1}) not only requires connecting the transformer system to the dielectric ES ceramic but also compromises the overall insulation performance of the system [14, 15]. This

 https://doi.org/10.1007/s40820-023-01290-4

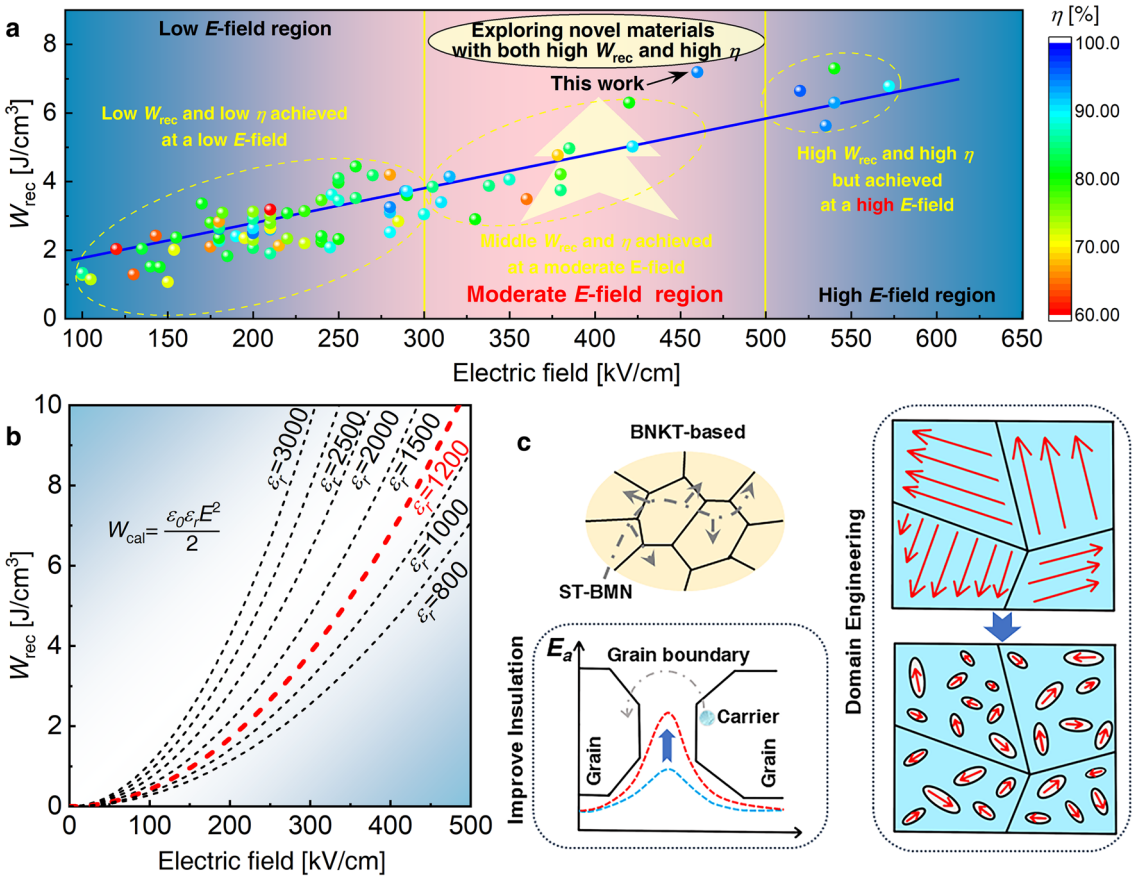

Fig. 1 **a** ES density and characteristics under varying *E*-fields. **b** The theoretical correlation between W_{rec} and *E*-field. **c** Enhanced insulation performance and domain structure of BNKT through ST-BMN doping

increases the system's cost while reducing its safety. Finding ceramic capacitors with high W_{rec} and η under low *E*-fields (300 kV cm^{-1}) can also be challenging. Therefore, it is imperative to explore innovative dielectric ceramics with high W_{rec} and η under moderate *E*-fields, as depicted in Fig. 1a. (2) Many studies have opted to delay saturation polarization to reduce ε_r and improve BDS [16, 17]. However, arbitrarily reducing ε_r can be detrimental. According to Eq. (4):

$$P = \varepsilon_0 \varepsilon_r E \tag{4}$$

where ε_0 is the vacuum permittivity. Extremely low ε_r diminishes macroscopic polarization, negatively impacting W_{rec} according to Eq. (2). Conversely, extremely high ε_r can lead to rapid polarization saturation and dielectric breakdown at low *E*-fields, reducing η. Therefore, understanding how to scientifically tailor ε_r is crucial. In Fig. 1b, we employed Eq. (5) to calculate the ESP of LD materials:

$$W_{cal} = \frac{\varepsilon_0 \varepsilon_r E^2}{2} \tag{5}$$

where W_{cal} is the theoretical calculated value of W_{rec}. As per Eq. (5), ES density is positively correlated with permittivity. However, RFEs are not linear dielectrics and exhibit substantial hysteresis, resulting in their W_{rec} typically being lower than W_{cal}. BDS, on the other hand, is associated with permittivity, with higher permittivity making breakdown easier under low *E*-fields, leading to lower ESP. To achieve ultrahigh ESP under a moderate *E*-field of 500 kV cm^{-1}, permittivity should be adjusted to around 1200, as shown in Fig. 1b.

Prior investigations suggest that lead-free bulk ES ceramics, comprising $BaTiO_3$ (BT)-based [18, 19], $(K_{0.5}Na_{0.5})NbO_3$ (KNN)-based [20, 21], and BNT-based materials, exhibit high P_{max} values [5, 22–24]. Particularly within BNT-based materials, P_{max} can surpass 40 μC cm^{-2} [18, 25, 26]. However, the strong hybridization between

the 6*s* orbital of Bi^{3+} ion and the 2*p* orbital of O^{2-} ion not only yields high P_{max} but also high P_r [27]. In our previous study, we introduced $SrTiO_3$ (ST) into BNT-based ceramics, where Sr^{2+} entered the A-site, inducing A-site disorder [28]. Although this reduces P_{max}, it significantly decreases ε_r. In this investigation, we counterbalance the negative impact on polarization by incorporating $Bi(Mg_{2/3}Nb_{1/3})O_3$ (BMN). On the one hand, this is conducive to enhancing P_{max} by introducing Nb^{5+} ions at the B-site and increasing the content of Bi^{3+} ions at the A-site. Calculations indicate that the activation energy (E_a) of grain boundaries rises with the increase in ST-BMN content. On the other hand, elevated E_a improves the material's insulating capabilities, as depicted in Fig. 1c. Additionally, the introduction of different ions into the A-site and B-site effectively disrupts long-range order through local *E*-field fluctuations [29, 30]. Based on the findings of T. Karthik et al. and Jing et al., it can be shown that $(Bi_{0.5}Na_{0.4}K_{0.1})TiO_3$ (referred to as BNKT) is situated in close proximity to the morphotropic phase boundary (MPB) [31, 32]. This particular positioning results in the manifestation of lower coercive field (E_c) and bigger polarization when compared to BNT. BNKT ceramics located near the MPB can transform macroscopic ferroelectric domains into polar nanoregions (PNRs), fostering increased η, and enhancing the materials' ESP. Consequently, under a moderate *E*-field, the (1–*x*)BNKT−*x*(2/3ST-1/3BMN) ceramics are anticipated to demonstrate superior ESP. Following the outlined strategy in Fig. 1, ST-BMN has been employed to modulate the domain, heighten the E_a of grain boundaries, and adjust the ε_r to approximately 1200. This approach aims to produce ceramic capacitors showcasing exceptional ESP within the range of moderate *E*-fields (300–500 kV cm^{-1}). Ultimately, a breakthrough in the performance of BNT-based materials has been achieved, attaining a W_{rec} of 7.19 J cm^{-3} and an ultrahigh η of 93.9% under a moderate *E*-field of 460 kV cm^{-1}, along with outstanding thermal stability spanning a temperature range of 30–140 °C.

2 Experimental Section

2.1 Sample Preparation

The conventional solid-state reaction technique, combined with the viscous polymer process, was employed for the fabrication of (1–*x*)BNKT−*x*(2/3ST-1/3BMN) ceramics, abbreviated as B-*x*SB, with *x* values of 0.35, 0.40, 0.45, and 0.50. The reactions and sintering were carried out at 880 and 1150 °C, respectively, for a duration of 2 h. Further details on the experimental procedures, encompassing sample preparation, structural characterization, and assessments of dielectric, ferroelectric, and ES properties, are provided in the Supplementary Information.

2.2 Structural Characterization

The phase structure was thoroughly examined using X-ray diffraction (XRD, Panalytical, Cambridge, UK) in the range of 10°–120°, with a sweeping rate of 2° min^{-1}, a working voltage of 45 kV, and a working current of 40 mA (operating conditions: Cu-Kα, $\lambda = 1.5418$ Å). Prior to testing, the sintered ceramic samples were ground into powders and annealed at 500 °C for 4 h to alleviate internal stress. The refinement of the phase structure was conducted using the FULLPROF software package (version 2000). The microstructure of the sintered samples was visualized using a scanning electron microscope (SEM, Quanta, FEG 250, FEI, Hillsboro, USA). Dark-field images, selected area electron diffraction (SAED) patterns, and nanoscale high-resolution images were acquired using a specialized aberration-corrected transmission electron microscope (AC-TEM, Talos F200X, FEI, USA).

2.3 Dielectric, Ferroelectric, and ES Properties Measurement

The temperature-dependent dielectric properties, encompassing ε_r and dielectric loss tangent (tanδ) of the investigated samples, were assessed using a multi-frequency LCR meter (E4980A, Agilent, Palo Alto, USA). The test parameters included a temperature range of 30–400 °C, a heating rate of 2 °C min^{-1}, and test frequencies spanning 0.3–1000 kHz, respectively. *P*–*E* hysteresis loops and *J*–*E* curves for all samples were acquired using the Sawyer–Tower circuit (TF analyzer 2000, Aachen, Germany). Prior to the first-order reversal curve (FORC) and charge–discharge testing, a 2-mm diameter electrode was affixed to the surface of the samples, each with a thickness of approximately 100 μm. The direct ESP of

 https://doi.org/10.1007/s40820-023-01290-4

the ceramic samples was evaluated using a charge–discharge testing system (CFD-003, TG Technology, Shanghai, China). W_{dis} and power density (P_D) were computed employing the formulas $W_{dis} = R\int i^2(t)dt/V$ and $P_D = EI_{max}/2S$, where $i(t)$, V, I_{max}, R, and S represent the time-dependent discharge current, effective volume, maximum discharge current, load resistance, and electrode area, respectively. FORC measurements were conducted using modulated triangle waveforms with a standard ferroelectric testing device (TF Analyzer 2000, aixACCT, Aachen, Germany). The Preisach density representing the distribution of FORC data was calculated from the descending segment of the primary hysteresis loop using a differential approach, as described by the following equation [33]:

$$\rho^{-}_{FORC}(E, E_r) = \frac{\partial^2 P^{-}_{FORC}(E, E_r)}{\partial E_r \partial E} \quad (5)$$

Here P^{-}_{FORC} denotes the polarization in the FORC analysis, E_r represents the reversal electric field, E is the actual applied electric field, and ρ^{-}_{FORC} signifies the Preisach density of the FORC distribution. The presence of the minus sign indicates that the FORC analysis commences from the descending branch of the primary hysteresis loop.

3 Results and Discussion

3.1 XRD Structural Characterization

The XRD patterns of B-*x*SB ceramic powders, with scanning angles 2θ ranging from 20° to 70°, are presented in Fig. 2a. All component diffraction peaks align with the BNT PDF #46-0001. Additionally, traces of a second phase were detected, with diffraction peaks potentially coinciding with the PDF #32-0118 of $Bi_2Ti_2O_7$, consistent with the previous findings [34, 35]. In Fig. 2b, the diffraction peaks at 39°–40.5° and 45.5°–47° are magnified. For $x > 0.45$, the (111) and (200) peaks shift toward lower angles, while others remain unchanged. To gain a deeper understanding, Rietveld refinement was employed to identify crystal symmetry and lattice characteristics. Table S2 and Fig. S1 summarize the fitting parameters. All B-*x*SB ceramic samples exhibit a coexistence of tetragonal (*T*) phase with *P*4*bm* space group and rhombohedral (*R*) phase with *R*3*c* space group, as demonstrated by the Rietveld refinement of B-0.5SB in Fig. 2c. Figure 2d shows that when $x \geq 0.45$, lattice parameters increase slightly, corresponding to the shift of (111) and (200) peaks.

ST and BMN form a solid solution with BNKT, allowing Sr^{2+} and Bi^{5+} to enter the A-site, according to our composition design. At a coordination number (CN) of 12, the ion radii of Sr^{2+} and Bi^{5+} are 144 and 130 pm, respectively [36]. Their radii in BNKT are between those of Bi^{5+} (130 pm), Na^{+} (139 pm), and K^{+} (164 pm). Therefore, A-site substitution does not result in an apparent lattice expansion. Both Mg^{2+} and Nb^{5+} ions enter the B-site simultaneously. With CN = 6, the radius of Ti^{4+} is 60.5 pm, while Nb^{5+} and Mg^{2+} are 64 and 72 pm, respectively. The radii of Nb^{5+} and Mg^{2+} ions are slightly larger than Ti^{4+}. When the doping level approaches 45% and 50%, Mg^{2+} replaces less than 10% of Ti^{4+} [36]. Therefore, when the doping amount increases to 45%, the crystal lattice slightly expands. However, when the doping quantity is too low, it does not generate an apparent lattice expansion, consistent with the previous results by Wang et al. [37] and Sun et al. [38]. As x increases from 0.35 to 0.50, the content of *R* phase increases somewhat and then declines, as shown in Fig. 2e. The *T* phase to *R* phase ratio remains nearly constant. The preservation of a strong polar phase is beneficial for maintaining macroscopic polarization. Figure 2f depicts the evolution of (111) and (200) diffraction peaks as the temperature rises from 30 to 100 °C. Due to the thermal expansion of the crystal lattice, these two peaks shift only toward lower angles with increasing temperature. The shape of these two peaks remains unchanged across the temperature range, indicating the coexistence of *R* and *T* phases from room temperature (RT) to 100 °C.

3.2 Dielectric Properties

The phase evolutions of the B-*x*SB ceramics were further assessed through their dielectric properties. The temperature-dependent ε_r of B-*x*SB ceramic samples, measured at various frequencies, is illustrated in Fig. 2g. In this temperature range, each composition exhibits two dielectric anomalies, a common occurrence in BNT-based systems [12, 28, 32, 39]. The dielectric anomaly with high dielectric dispersion on the left is attributed to a normal dielectric relaxation, while the broad dielectric peak with low dielectric dispersion on the right is associated with a diffuse phase transition caused by the coexistence of *R* and *T* phases [40, 41] or a transformation from low-temperature PNRs to

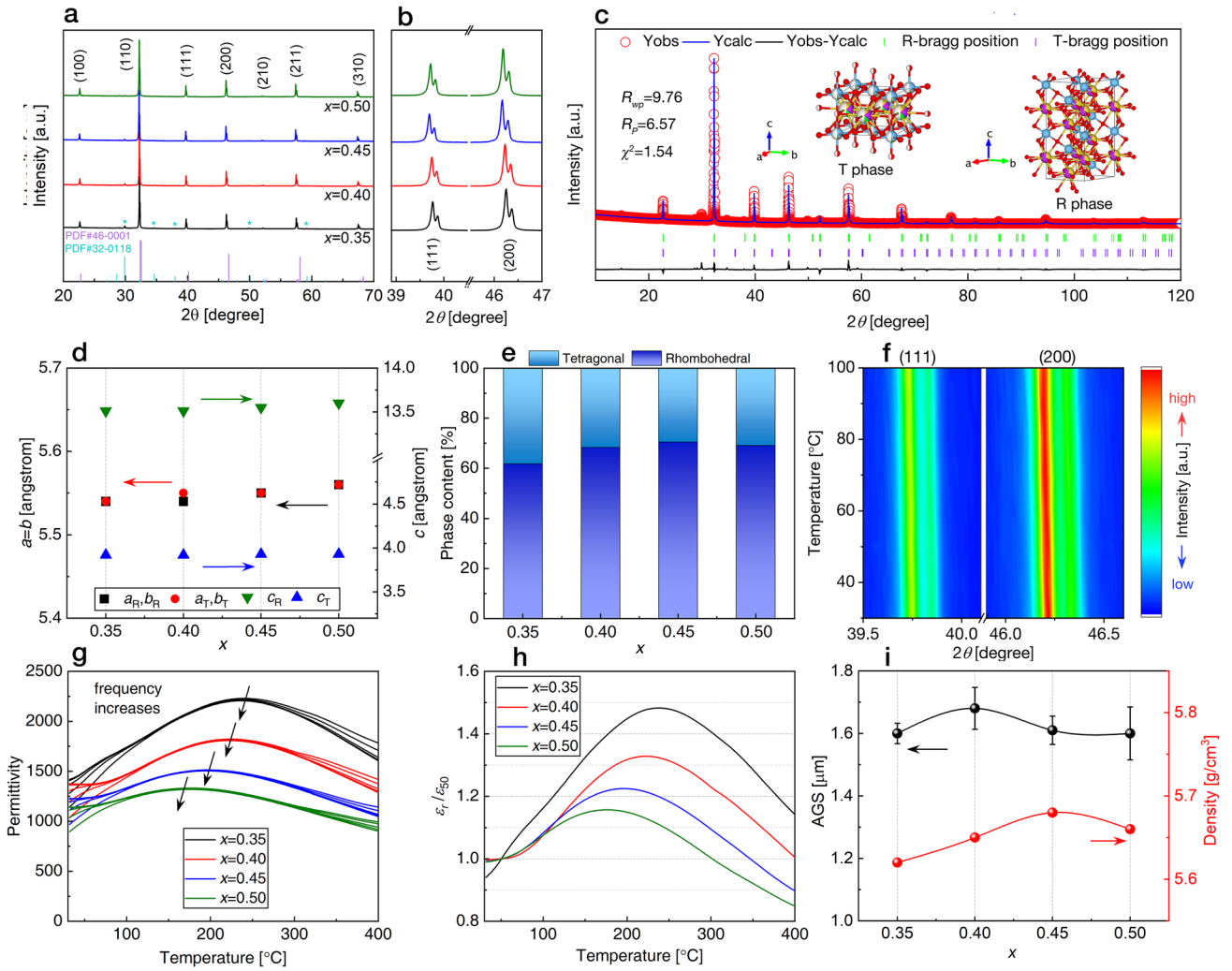

Fig. 2 **a** XRD pattern of ceramics with varying x (0.35, 0.40, 0.45, and 0.50) in the 20°–70° range. **b** Enlarged views of the diffraction peaks at 39°–40.5° and 45.5°–47°. **c** Fitted XRD pattern for $x=0.50$ ceramic powders. **d** Variation of lattice parameters with x for B-xSB ceramics. **e** Proportion variation of the R and T phases for different compositions. **f** Temperature evolution of XRD patterns for $x=0.50$ ceramic from 30 to 100 °C at selected angles of 39.5°–40° and 46°–46.5°. **g** Temperature-dependent ε_r and tanδ for $x=0.35$, 0.40, 0.45, and 0.50 at measurement frequencies of 0.3, 1, 10, 100, and 1000 kHz, ranging from 30 to 400 °C. The long arrow indicates the direction of increasing measurement frequency. **h** $\varepsilon_r/\varepsilon_{50}$ as a function of temperature measured at 1 kHz, where ε_{50} was measured at 50 °C, and ε_r was measured from 30 to 400 °C. **i** AGS and density variations with x for B-xSB ceramics

high-temperature PNRs [28, 42–44]. The dielectric anomaly peak on the left shifts toward higher temperatures with increasing frequency, indicative of a typical RFE characteristic [45, 46]. The temperature (T_m) at which the maximum permittivity (ε_m) occurs demonstrates a clear shift toward lower values as x increases from 0.35 to 0.5. This behavior can be attributed to the disruption of the long-range ferroelectric order and the simultaneous increase in PNRs content. Notably, ε_r decreases with increasing BMN concentration, reaching the lowest value for the $x=0.50$ composition. The curves of $\varepsilon_r/\varepsilon_{50}$ (where ε_{50} is the ε_r measured at 1 kHz and 50 °C) with increasing temperature are depicted in Fig. 2h. The $x=0.50$ composition exhibits the lowest and most stable $\varepsilon_r/\varepsilon_{50}$, signifying superior temperature stability. Due to its low ε_r and excellent temperature stability, this composition holds great appeal for dielectric capacitor applications.

https://doi.org/10.1007/s40820-023-01290-4

3.3 Surface Microstructures

SEM was employed to unveil the microstructures of B-*x*SB ceramics. In Fig. 2i, the average grain size (AGS) and density of B-*x*SB ceramics are depicted. The AGS and density exhibit slight variations with increasing BMN concentration, measuring between 1.60 and 1.68 μm and between 5.62 and 5.68 g cm^{-3}, respectively. The surface morphologies of B-*x*SB ceramic samples, shown in Fig. 3a1–d1, reveal dense structures with minimal porosity. While no obvious second phase is observed in Fig. 3a1–b1, a small amount of second phase is apparent in Fig. 3c1–d1. As suggested by the XRD data, these second-phase materials are highly correlated to an oxide formed by the precipitation of Bi and Ti. This phenomenon of Bi precipitation is a recurring observation in BNT-based materials. Despite our concerted efforts to mitigate Bi precipitation during the sintering process through various methods, a minor amount of precipitation remains. It is important to note that similar observations of Bi precipitation have been documented in prior studies focusing on BNT-based materials [34, 35]. This phenomenon seems to be a common characteristic within this class of materials. The statistical diagrams of grain size distribution, presented in Fig. 3a2–d2, indicate that all grain size distributions follow a normal distribution.

Combining surface morphology and permittivity, we simulated the applied *E*-field to investigate potential distribution and local *E*-field distribution. SEM was utilized to individually portray grains and grain boundaries, and the ε_r intensity map is provided in Fig. 3a3–d3. Figure 3a4–d4 illustrates the potential distribution after simulating an external *E*-field of 150 kV cm^{-1} downward. It is evident that as *x* increases, the potential difference between grains decreases significantly. As shown in Fig. 3a5–d5 (local *E*-field distribution), the regions represented by white circles exhibit the greatest potential difference and are more likely to experience breakdown, particularly at grain boundaries, elucidating the ceramics' susceptibility to grain boundary breakdown. When $x = 0.50$, the breakdown resistance performance improves. Moreover, the impedance of B-*x*SB ceramics was measured between 430 and 530 °C, as depicted in Fig. 3a6–d6. The grain boundary resistance was calculated using the (CR) (CR) model fitting, and E_a was determined using the Arrhenius formula [47]:

$$\sigma = A \cdot e^{\frac{-E_a}{k_B \cdot T}} \quad (6)$$

where σ is conductivity, A is a constant, k_B is the Boltzmann constant, and T is temperature. Taking the derivative on both sides of the formula yields E_a. The results indicate that as ST-BMN concentrations increase, E_a rises from 0.90 eV ($x = 0.35$) to 1.21 eV ($x = 0.50$). The larger E_a inhibits carriers from crossing grain boundaries, effectively enhancing material insulation. These findings lay the groundwork for improving BDS.

3.4 Nanoscale Microstructures

The nanoscale microstructures of the $x = 0.50$ composition were meticulously examined using an AC-TEM. The bright-field image of a sample prepared through focused ion beam (FIB) is presented in Fig. 4a. High-resolution (HR)-TEM images of the $x = 0.50$ composition are detailed in Fig. 4b, where the distribution of cations is reflected by the imaging brightness. At the A-site, the brightness of Na^+, Bi^{3+}, K^+, and Sr^{2+} cations is comparatively high, while at the B-site, the brightness of Nb^{5+}, Mg^{2+}, and Ti^{4+} cations is low. The brightness distribution is further illustrated in Fig. 4c insert, with high brightness in red and low brightness in blue. Figure 4c distinctly reveals the distribution of cations on the B-site (in yellow and green). The coordinates of the A-site atoms are extracted using the red region's coordinates, and the theoretical coordinates of B-site atoms are calculated. Subsequently, the actual coordinates of B-site atoms are extracted based on the coordinates of the yellow and green regions, facilitating the simulation of the spontaneous polarization vector in each cell, as depicted in Fig. 4d. The background in Fig. 4d is an intensity map of polarization, showcasing the random orientation of spontaneous polarization vectors in each cell. Different colors represent polarization vectors in different directions, a characteristic of RFE, forming the basis for unique properties and the chemical foundation for the existence of PNRs. The strong polar and weak polar regions, depicted in dark blue and light blue backgrounds, respectively, are randomly distributed, and the dipoles within the white circle exhibit the same orientation, indicating PNRs. All PNRs have a diameter of less than 5 nm, indicating effective refinement by local *E*-field fluctuations, which enhances the ESP of the material [48–50].

Figure 4e and f shows selected area electron diffraction (SAED) patterns along $[110]_{pc}$ and $[111]_{pc}$, where pc

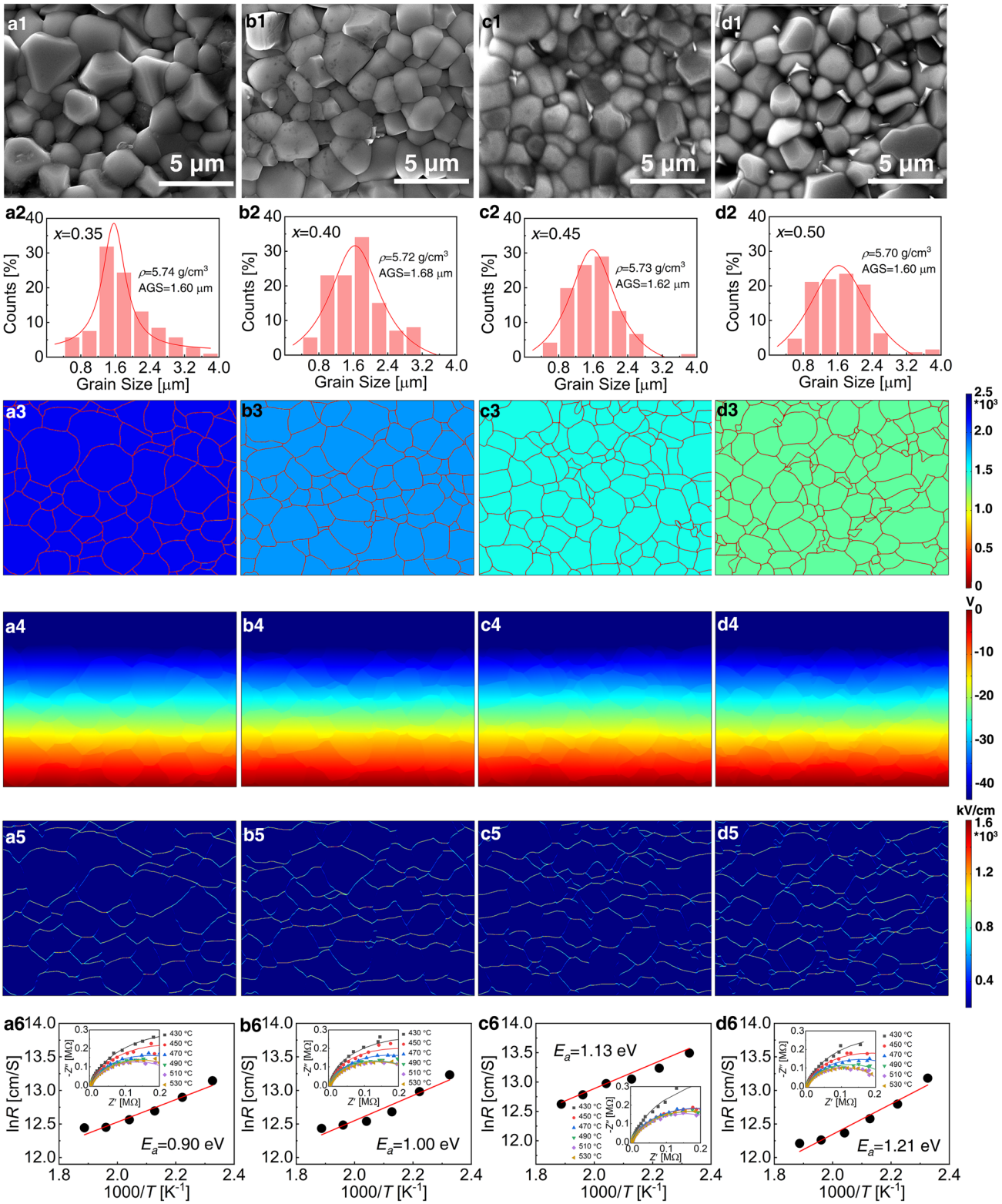

Fig. 3 SEM images of surface morphologies for compositions **a1** $x=0.35$, **a2** $x=0.40$, **a3** $x=0.45$, and **a4** $x=0.50$ ceramics. **a2–d2** Grain size distribution. **a3–d3** Intensity mapping of ε_r. **a4–d4** Distribution of electric potentials. **a5–d5** Local *E*-field distribution. **a6–d6** Relationship between temperature (T) and grain boundary resistance, with resistance spectra shown in the insets

https://doi.org/10.1007/s40820-023-01290-4

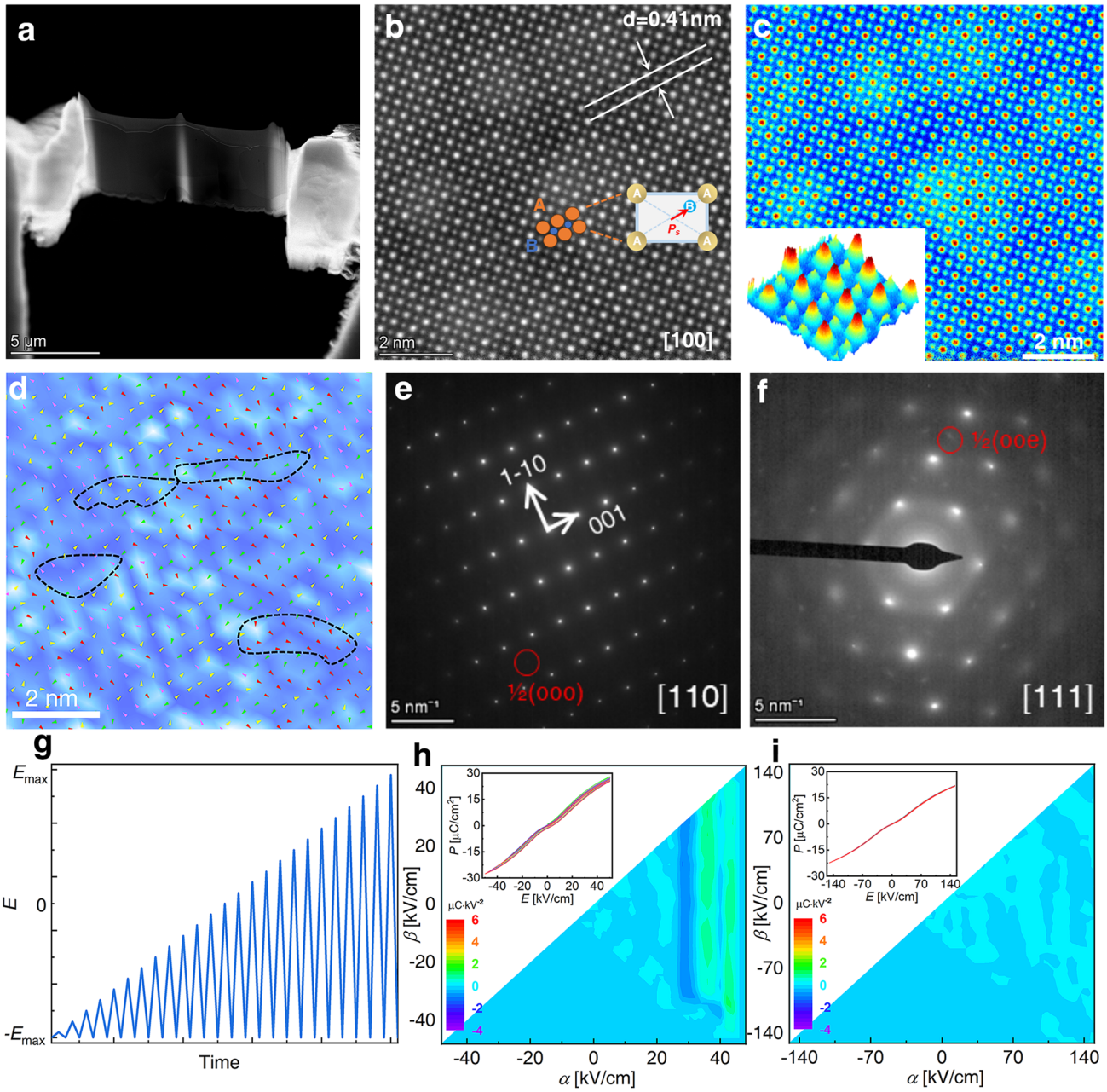

Fig. 4 **a** Bright-field and **b** high-resolution TEM image of BSB-0.5 ceramic. **c** Redistribution of brightness based on the RGB values of **b**. **d** The polarization vector, calculated from cation displacement on the B-site, superimposed on the polarization intensity distribution, with relative polarization intensity expressed through the brightness and saturation of the background color. SAED patterns along **e** $[110]_{pc}$ and **f** $[111]_{pc}$. **g** FORC test method. Evolution of FORC distributions for **h** $x=0.35$ and **i** $x=0.50$

denotes pseudo-cubic. The presence of 1/2(ooo) superlattice points in [110] indicates the R phase, while the presence of 1/2(ooe) superlattice points in [111] indicates the T phase [51]. These patterns confirm that the composition with $x=0.50$ possesses a phase structure consisting of coexisting R and T phases, consistent with the Rietveld fitting result of XRD. While TEM can reveal domain morphologies at the nanometer scale, it typically provides static results. In contrast, piezoresponse force microscopy (PFM) elucidates polarization switching behavior at the micrometer scale but faces challenges in capturing dynamic details, especially in relaxor ferroelectrics [52]. In these materials, PNRs rather

than macroscopic domains respond to external driving fields. The switching behavior of individual PNR may vary due to local electric field variations, and historical responses can influence polarization switching behavior. FORC analysis is a valuable technique that can detect a range of residual states dependent on field history. It effectively represents the reaction of local structures in the presence of a uniform electric field and provides a statistical outcome of polarization switches in *P*–*E* loops. This approach incorporates spatial and historical polarization dynamics, offering direct insights into microstructures [53, 54]. FORCs of $x = 0.35$ and 0.50 ceramics were examined to illustrate macroscopically that in a sample with $x = 0.50$, all domains are converted into microscopic PNRs. Figure 4g and h–i depicts the principle and FORCs of ceramics with $x = 0.35$ and 0.50, respectively. In simpler terms, FORC is employed to quantify the number of polarization reversals: A higher value indicates more reversals, while a lower value signifies fewer reversals. The motion of domain barriers is recorded by tracking changes in domains through polarization reversals. In low *E*-fields, the low number of ferroelectric phases and the strong nonlinear polarization behavior of $x = 0.35$ ceramics at 30 kV cm^{-1} indicate the inversion of ferroelectric domains and the movement of domain walls. This significant hysteresis is a consequence of weak ESP. Even when the sample with $x = 0.50$ is loaded to 150 kV cm^{-1}, there is no high-intensity distribution, indicating that ferroelectricity is diluted, RFE features are enhanced, and hysteresis is diminished. This is consistent with the exclusive discovery of tiny PNRs by TEM.

3.5 Ferroelectric and ES Performance

Subsequently, the ferroelectric and ES properties of B-*x*SB ceramic samples were thoroughly assessed. Figure 5a illustrates the unipolar *P*–*E* hysteresis loops of B-*x*SB samples with $x = 0.35$, 0.40, 0.45, and 0.50. Owing to the decrease in ε_r, the E_{max} that can be applied to the sample before electrical breakdown increases with the rising values of *x*. For B-*x*SB samples with *x* ranging from 0.35 to 0.50, the respective E_{max} values are 310, 330, 430, and 460 kV cm^{-1} at a test frequency of 10 Hz. All B-*x*SB samples exhibited slim hysteresis loops, characteristic of RFE ceramics [9]. As *x* increases, the *P*–*E* loops become slimmer. Corresponding *J*–*E* curves are presented in Fig. 5b, revealing two distinct current peaks at 50 kV cm^{-1}. The RFE nature of B-*x*SB samples disrupts long-range ferroelectric order, resulting in the appearance of PNRs. When an applied *E*-field is present, PNRs become oriented but are unable to grow into macrodomains and return to random orientation when the *E*-field drops from E_{max} to zero. Consequently, the *J*–*E* curves exhibit twin peaks at low *E*-fields. Given the ruled-out AFE nature of BNT-based solid solutions [55, 56], the very slim *P*–*E* loops combined with double current peaks in *J*–*E* curves should be described as an AFE-like RFE (AL-RFE) characteristic [8, 57], rather than a relaxor AFE characteristic [58–60]. Furthermore, Fig. 5b indicates that these two current maxima are roughly symmetric and remain fairly constant as *x* increases. It is noteworthy that the P_{max} determined at the same E_{max} gradually decreases as *x* increases from 0.35 to 0.50, owing to the decoupling of A-O and B–O bonds [61]. However, the Pmax of B-*x*SB ceramic samples evaluated at their respective E_{max} exhibits negligible variation versus *x*. This suggests that the loss of P_{max} due to the decoupling effect can be compensated for by increasing E_{max}. Figure 5a also reveals that the P_r has decreased from 2.64 ($x = 0.35$) to 0.015 ($x = 0.50$) μC cm^{-2}, allowing the ΔP and W_{rec} to grow. W_{rec} and η are determined using the unipolar *P*–*E* loops shown in Fig. 5a. When the E_{max} increases by 48% from 310 kV cm^{-1} ($x = 0.35$) to 460 kV cm^{-1} ($x = 0.50$), the W_{rec} increases by 67% from 4.30 J cm^{-3} ($x = 0.35$) to 7.19 J cm^{-3} ($x = 0.50$), while the η of B-*x*SB ceramic samples remains around 90%. This result indicates that the $x = 0.50$ composition has superior ESP than the other three compositions. Consequently, Fig. 5d depicts the comprehensive *P*–*E* loops and corresponding *J*–*E* curves of the $x = 0.50$ composition measured from 50 to 460 kV cm^{-1}. Under a small *E*-field, the *J*–*E* curves exhibit a rectangular form. Due to the *E*-field-induced RFE-to-polar phase transition [27, 56], double current maxima are observed in the *J*–*E* curves when the *E*-field exceeds 150 kV cm^{-1}. The field corresponding to these two maximum values of current scarcely fluctuates, demonstrating that even if the *E*-field is increased to E_{max}, the critical *E*-field for RFE-to-polar phase transition will remain unchanged. More crucially, as the *E*-field grows, the *P*–*E* loops remain slim and do not broaden, indicating that no conductive process has been activated, and a high η can be achieved. Figure 5e depicts the W_{rec} and η of the $x = 0.50$ composition under various *E*-fields. The W_{rec} grows monotonously and reaches an impressive value of 7.19 J cm^{-3} at 460 kV cm^{-1}, whereas

 https://doi.org/10.1007/s40820-023-01290-4

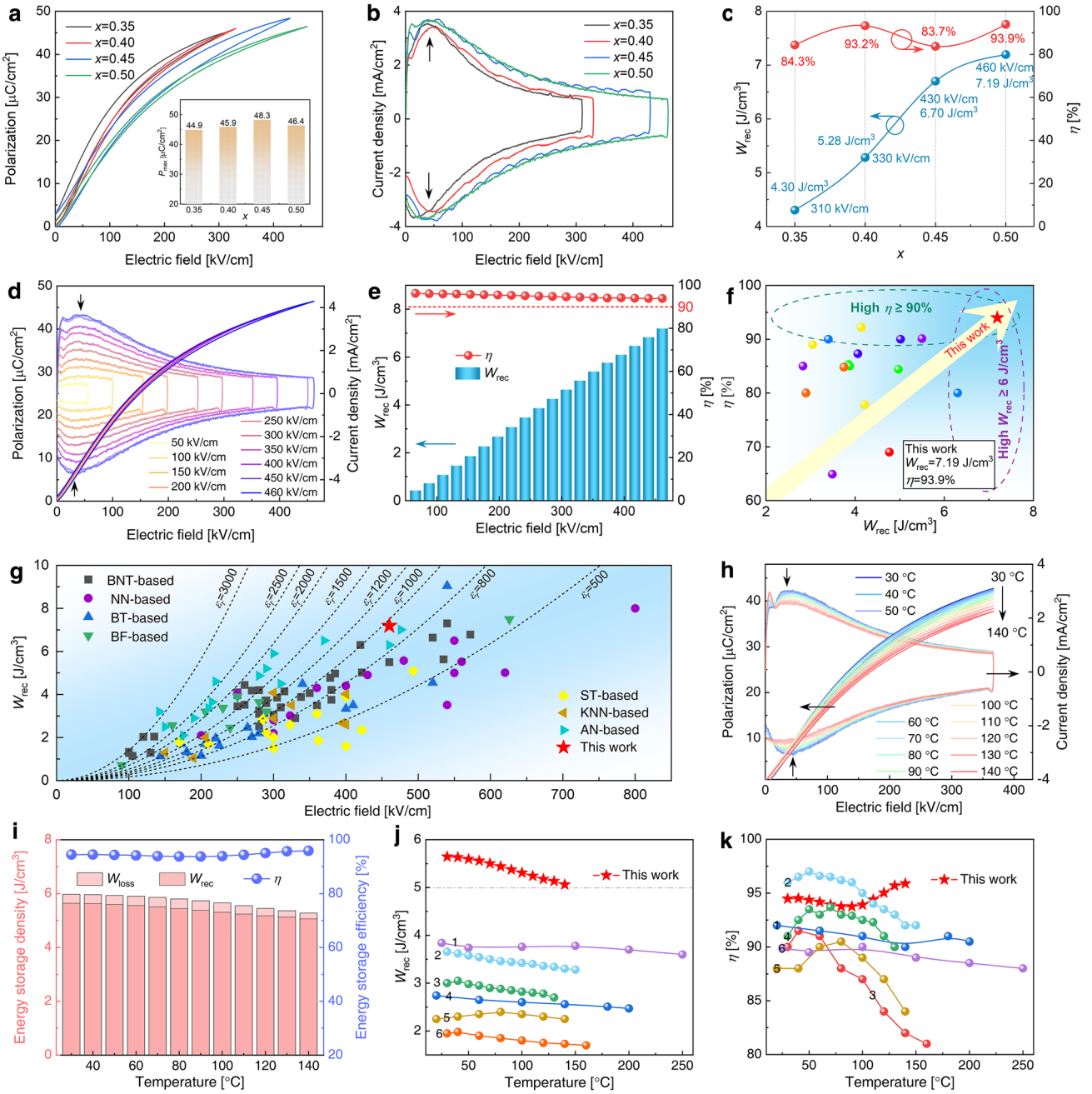

Fig. 5 **a** *P–E* loops and **b** the corresponding current density–electric field (*J–E*) curves for $x=0.35$, 0.40, 0.45, and 0.50, measured at RT, 10 Hz, and various *E*-fields. **c** W_{rec} and η of $x=0.35$, 0.40, 0.45, and 0.50 ceramics. BDS is indicated next to the data. **d** *P–E* loops and corresponding *J–E* curves for $x=0.50$ composition measured at RT and 10 Hz. **e** W_{rec} and η of $x=0.50$ composition. **f** Comparison of W_{rec} and η for BSB-0.50 and other BNT-based bulk ceramics. **g** Comparison of W_{rec} for B-0.5SB ceramic with other bulk ceramics. **h** *P–E* loops and *J–E* curves of B-0.5SB ceramic measured at 10 Hz and 366 kV cm^{-1}. Temperature increases from 30 to 140 °C in steps of 10 °C. **i** W_{loss}, W_{rec}, and η calculated from the corresponding *P–E* loops of B-0.5SB. Temperature-dependent W_{rec} **j** and η (k) of B-0.5SB compared with other BNT-based bulk ceramics

the η shows very little reduction and still maintains a very high value of 94% at the same *E*-field.

Figure 5f compares the ESP of the $x=0.50$ ceramic with that of other BNT-based bulk ceramics [25, 62–78]. Details regarding the composition, E_{max}, W_{rec}, and η of the compared BNT-based bulk ceramics are summarized in Table S3. Clearly, the ESP of the $x=0.50$ composition surpasses that of existing BNT-based ceramics.

Generally, increasing the *E*-field improves W_{rec}. However, in the high *E*-field region, it appears that augmenting the electric field does not directly enhance W_{rec}. Although the E_{max} values of 0.8BNT-0.2Sr($Nb_{0.5}Al_{0.5}$)O_3 [74] and 0.85[0.7BNT–0.3($Bi_{0.1}Sr_{0.85}$)TiO_3]–0.15$KNbO_3$ [72] ceramics are 520 and 569 kV cm^{-1}, respectively, their W_{rec} values are 6.64 and 5.63 J cm^{-3}, which are inferior to the W_{rec} of our ceramic. Conversely, even with high W_{rec} values of 7.02 and 6.3 J cm^{-3} at 390 and 420 kV cm^{-1}, the η values of 0.78BNT-0.22$NaNbO_3$ [65] and 0.85(0.94BNT-0.06BT)-0.15Bi($Mg_{2/3}Nb_{1/3}$)O_3 [25] ceramics, at 85% and 80% respectively, are significantly lower than our ceramic (94%). Consequently, we achieve a comprehensive improvement in ESP with both high W_{rec} and high η in the $x = 0.50$ ceramic sample. In Fig. 5g, the ESP of the $x = 0.50$ ceramic is compared to that of various representative dielectric ceramic materials, including linear ST-based systems, AFE $AgNbO_3$ (AN)-based and $NaNbO_3$ (NN)-based systems, and RFE BT-based, KNN-based, BF-based, and BNT-based systems. Details of the composition, E_{max}, W_{rec}, and η of the compared systems, are summarized in Table S4. It is evident that linear ST-based systems often have low W_{rec} (< 4 J cm^{-3}), but AFE AN-based and NN-based systems exhibit higher W_{rec} (4–7 J cm^{-3}) and low η (50–90%). In contrast, RFE BT-based and KNN-based systems show medium W_{rec} (2–4 J cm^{-3}) and fluctuating η (50–95%) under a moderate *E*-field. Although some BNT-based systems achieve higher W_{rec} and very high η (> 90%), the E_{max} has approached 520–600 kV cm^{-1}. In contrast, our $x = 0.50$ composition exhibits high W_{rec} (> 7 J cm^{-3}) and high η (94%) simultaneously at a moderate E_{max} (460 kV cm^{-1}), indicating a comprehensive improvement in ESP. These findings demonstrate that by manipulating ε_r, we were able to create B-*x*SB ceramics with exceptional ESP in a moderate *E*-field. As a result, it has emerged as one of the most promising candidate materials for pulse ES ceramic devices.

Temperature stability is a critical criterion for pulse ES ceramic devices [79, 80]. The temperature stability of the ESP for the $x = 0.50$ composition was evaluated using temperature-dependent *P*–*E* and *J*–*E* curves, as illustrated in Fig. 5h. These curves were measured at 365 kV cm^{-1} and 10 Hz, with temperatures ranging from 30 to 140 °C. Typically, in RFEs, P_r and E_c increase with rising temperature due to thermal activation of defects, which is detrimental to the stability of W_{rec} and η [7, 9, 81]. As the temperature increases, the *P*–*E* loops remain thin, and P_{max} decreases slightly from 42.7 to 37.0 μC cm^{-2}. The two current peaks indicated by the black arrows show almost no movement with rising temperature. These findings suggest that the ESP in the $x = 0.50$ composition exhibits good thermal stability. Despite a slight reduction in temperature, the W_{rec} of the $x = 0.50$ composition decreases from 5.64 J cm^{-3} at 30 °C to 5.06 J cm^{-3} at 140 °C, a 10% reduction, as shown in Fig. 5i. Because the P_r and E_c of the $x = 0.50$ composition remained reasonably steady, its η is extraordinarily high, with minimal variations ranging from 93.9 to 95.9%. The temperature-dependent ESP of the $x = 0.50$ composition is compared to other previously reported BNT-based ceramics in Fig. 5j–k [62, 64, 65, 74, 82, 83]. The constituents of these BNT-based ceramics are summarized in Table S5 (see Supplementary Information). The W_{rec} in those BNT-based ceramics typically declines to some extent as temperature rises, with none exceeding 4 J cm^{-3}. In contrast, the W_{rec} of our $x = 0.50$ composition is significantly higher than the values of various BNT-based ceramics in the 30–140 °C temperature range, surpassing 5 J cm^{-3} at this temperature range, as shown in Fig. 5j. Furthermore, upon comparing the η, it is evident that the η of the $x = 0.50$ composition remains around 95%. Even with rising temperature, the trend is upward, as illustrated in Fig. 5k. In conclusion, in addition to the ultrahigh ESP at RT, the ESP of the $x = 0.50$ composition demonstrates ultrahigh W_{rec} and exceptional η over a wide temperature range, outperforming other BNT-based ceramics.

3.6 Charge–Discharge Performance

Finally, we evaluate the charge–discharge performance of the $x = 0.50$ composition, a pivotal criterion for pulse capacitor devices [84]. The sample thickness is 100 μm, and the electrode area is 3.14 mm^2. Charge–discharge tests employ a 100-Ω resistor. A dielectric ceramic with rapid charge/discharge characteristics is well-suited for pulse power supply. Room temperature electric current versus time (*I*–*t*) curves measured in an overdamped discharge mode are presented in Fig. 6a. The I_{max} increases with the escalating electric field. W_{dis} attains its peak value of 3.89 J cm^{-3} under 400 kV cm^{-1}, as depicted in Fig. 6b. The time at which W_{dis} releases 90% of its total energy, often denoted as $t_{0.9}$, is crucial for calculating discharge speed. At 100 kV cm^{-1}, the $t_{0.9}$ for the $x = 0.50$ composition is approximately 0.21 μs, diminishing with increasing electric field. At 400 kV cm^{-1},

 https://doi.org/10.1007/s40820-023-01290-4

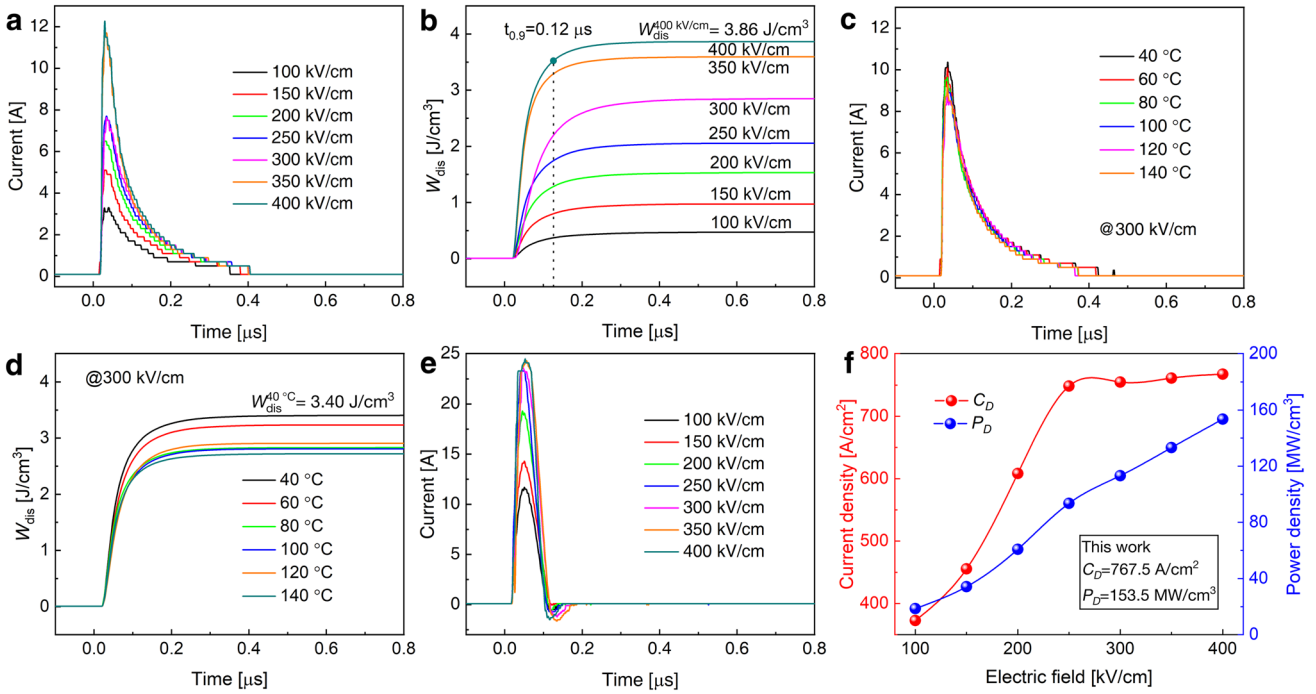

Fig. 6 Pulsed overdamped discharging properties of B-0.5SB bulk ceramics, illustrating **a** current curves and **b** W_{dis} at RT and various electric fields. Temperature-dependent pulsed overdamped discharging properties of B-0.5SB bulk ceramics, depicting **c** current curves and **d** W_{dis} at 300 kV cm^{-1} as the temperature increases from 40 to 140 °C in intervals of 20 °C. Pulsed underdamped discharging properties of B-0.5SB bulk ceramics, exhibiting **e** current curves, and **f** C_D and P_D as functions of the electric field at RT

$t_{0.9}$ is less than 0.12 μs. Figure 6c illustrates the temperature-dependent *I*–*t* curves from 40 to 140 °C, determined at overdamped discharge mode under an *E*-field of 300 kV cm^{-1}. The $t_{0.9}$ remains below 0.13 μs at all measured temperatures, as demonstrated in Fig. 6d. The *I*–*t* curves of underdamped discharge at different *E*-fields are presented in Fig. 6e, and the calculated current density (C_D) and power density (P_D) are displayed in Fig. 6f. The discharge of the $x = 0.50$ composition is confirmed to be complete after only two oscillations. At 400 kV cm^{-1}, C_D and P_D are exceedingly high at 767.5 A cm^{-2} and 153.5 MW cm^{-3}, respectively. These features indicate that the $x = 0.50$ composition ceramics exhibit significant potential for use in pulse power devices [7, 82].

4 Conclusions

In summary, we propose an approach to achieve optimal ESP under constrained *E*-field conditions by tailoring the ε_r. Ultimately, the $x = 0.50$ composition demonstrates an extraordinary η of 93.8% and an impressive W_{rec} of 7.19 J cm^{-3} at a moderate *E*-field. The temperature-dependent ESP of the $x = 0.50$ composition is also notably robust. Across the temperature range of 30–140 °C, W_{rec} consistently exceeds 5 J cm^{-3} with high efficiency (above 95%). In contrast with other BNT-based bulk ceramic capacitors, the B-0.5SB ceramic, with its exceptional ESP, undoubtedly stands out as a promising candidate for future ES devices. Moreover, the B-0.5SB ceramic exhibits an ultrahigh current density and power density, simulating real-world application scenarios. Although this study employed linear dielectrics as a model and acknowledges some discrepancies between research results and theoretical conclusions, it addresses a crucial research gap concerning the attainment of high ESP in a restricted *E*-field. To conclude, this strategy, involving the modification of ε_r, enhancement of insulating properties, and incorporation of domain engineering, proves effective. It is anticipated that these findings will contribute to and guide future research and development endeavors in the realm of ceramic capacitors.

Acknowledgements This work was supported by the National Natural Science Foundation of China (Grant No. 51761145024),

the Key Research and Development Program of Shaanxi (Program No. 2022KWZ-22), the Natural Science Basic Research Program of Shaanxi (Program No. 2023-JC-YB-441), the Youth Innovation Team of Shaanxi Universities, and the Fundamental Research Funds of Shaanxi Key Laboratory of Artificially-Structured Functional Materials and Devices (AFMD-KFJJ-21203). The research was made possible by Russian Science Foundation (Project No. 23-42-00116). The equipment of the Ural Center for Shared Use "Modern nanotechnology" Ural Federal University (Reg. No. 2968) which is supported by the Ministry of Science and Higher Education RF (Project No. 075-15-2021-677) was used. The SEM work was done at International Center for Dielectric Research (ICDR), Xi'an Jiaotong University, Xi'an, China. The authors also thank Shiyanjia Lab (www.shiyanjia.com/paperaward.html) for providing assistance with TEM characterization.

Declarations

Conflict of interest The authors declare no interest conflict. They have no known competing financial interests or personal relationships that could have appeared to influence the work reported in this paper.

Supplementary Information The online version contains supplementary material available at https://doi.org/10.1007/s40820-023-01290-4.

References

1. Z. Yao, Z. Song, H. Hao, Z. Yu, M. Cao et al., Homogeneous/inhomogeneous-structured dielectrics and their energy-storage performances. Adv. Mater. **29**, 1601727 (2017). https://doi.org/10.1002/adma.201601727
2. J. Li, F. Li, Z. Xu, S. Zhang, Multilayer lead-free ceramic capacitors with ultrahigh energy density and efficiency. Adv. Mater. **30**, 1802155 (2018). https://doi.org/10.1002/adma.201802155
3. J. Li, Z. Shen, X. Chen, S. Yang, W. Zhou et al., Grain-orientation-engineered multilayer ceramic capacitors for energy storage applications. Nat. Mater. **19**, 999–1005 (2020). https://doi.org/10.1038/s41563-020-0704-x
4. L. Yang, X. Kong, F. Li, H. Hao, Z. Cheng et al., Perovskite lead-free dielectrics for energy storage applications. Prog. Mater. Sci. **102**, 72–108 (2019). https://doi.org/10.1016/j.pmatsci.2018.12.005
5. G. Wang, Z. Lu, Y. Li, L. Li, H. Ji et al., Electroceramics for high-energy density capacitors: current status and future perspectives. Chem. Rev. **121**, 6124–6172 (2021). https://doi.org/10.1021/acs.chemrev.0c01264
6. Z. Yang, H. Du, L. Jin, D. Poelman, High-performance lead-free bulk ceramics for electrical energy storage applications: design strategies and challenges. J. Mater. Chem. A **9**, 18026–18085 (2021). https://doi.org/10.1039/D1TA04504K
7. G. Liu, Y. Li, B. Guo, M. Tang, Q. Li et al., Ultrahigh dielectric breakdown strength and excellent energy storage performance in lead-free Barium titanate-based relaxor ferroelectric ceramics via a combined strategy of composition modification, viscous polymer processing, and liquid-phase sintering. Chem. Eng. J. **398**, 125625 (2020). https://doi.org/10.1016/j.cej.2020.125625
8. L. Zhang, R. Jing, Y. Huang, Q. Hu, D.O. Alikin et al., Enhanced antiferroelectric-like relaxor ferroelectric characteristic boosting energy storage performance of $(Bi_{0.5}Na_{0.5})TiO_3$-based ceramics via defect engineering. J. Materiomics **8**, 527–536 (2022). https://doi.org/10.1016/j.jmat.2022.01.007
9. L. Jin, F. Li, S. Zhang, Decoding the fingerprint of ferroelectric loops: comprehension of the material properties and structures. J. Am. Ceram. Soc. **97**, 1–27 (2014). https://doi.org/10.1111/jace.12773
10. H.Y. Zhou, X.Q. Liu, X.L. Zhu, X.M. Chen, $CaTiO_3$ linear dielectric ceramics with greatly enhanced dielectric strength and energy storage density. J. Am. Ceram. Soc. **101**, 1999–2008 (2018). https://doi.org/10.1111/jace.15371
11. H. Wang, Y. Liu, T. Yang, S. Zhang, Ultrahigh energy-storage density in antiferroelectric ceramics with field-induced multiphase transitions. Adv. Funct. Mater. **29**, 1807321 (2019). https://doi.org/10.1002/adfm.201807321
12. J. Lv, Q. Li, Y. Li, M. Tang, D. Jin et al., Significantly improved energy storage performance of NBT-BT based ceramics through domain control and preparation optimization. Chem. Eng. J. **420**, 129900 (2021). https://doi.org/10.1016/j.cej.2021.129900
13. L. Zhang, M. Zhao, Y. Yang, Y. Li, M. Tang et al., Achieving ultrahigh energy density and ultrahigh efficiency simultaneously via characteristic regulation of polar nanoregions. Chem. Eng. J. **465**, 142862 (2023). https://doi.org/10.1016/j.cej.2023.142862
14. H. Palneedi, M. Peddigari, G.-T. Hwang, D.-Y. Jeong, J. Ryu, High-performance dielectric ceramic films for energy storage capacitors: progress and outlook. Adv. Funct. Mater. **28**, 1803665 (2018). https://doi.org/10.1002/adfm.201803665
15. L. Chen, H. Yu, J. Wu, S. Deng, H. Liu et al., Large energy capacitive high-entropy lead-free ferroelectrics. Nano-Micro Lett. **15**, 65 (2023). https://doi.org/10.1007/s40820-023-01036-2
16. J. Shi, Y. Zhao, J. He, T. Li, F. Zhu et al., Deferred polarization saturation boosting superior energy-storage efficiency and

density simultaneously under moderate electric field in relaxor ferroelectrics. ACS Appl. Energy Mater. **5**, 3436–3446 (2022). https://doi.org/10.1021/acsaem.1c04017

17. J. Zhao, T. Hu, Z. Fu, Z. Pan, L. Tang et al., Delayed polarization saturation induced superior energy storage capability of $BiFeO_3$-based ceramics via introduction of non-isovalent ions. Small **19**, e2206840 (2023). https://doi.org/10.1002/smll.202206840
18. W. Wang, L. Zhang, R. Jing, Q. Hu, D.O. Alikin et al., Enhancement of energy storage performance in lead-free Barium titanate-based relaxor ferroelectrics through a synergistic two-step strategy design. Chem. Eng. J. **434**, 134678 (2022). https://doi.org/10.1016/j.cej.2022.134678
19. W. Wang, L. Zhang, C. Li, D.O. Alikin, V.Y. Shur et al., Effective strategy to improve energy storage properties in lead-free $(Ba_{0.8}Sr_{0.2})TiO_3$-$Bi(Mg_{0.5}Zr_{0.5})O_3$ relaxor ferroelectric ceramics. Chem. Eng. J. **446**, 137389 (2022). https://doi.org/10.1016/j.cej.2022.137389
20. X. Ren, L. Jin, Z. Peng, B. Chen, X. Qiao et al., Regulation of energy density and efficiency in transparent ceramics by grain refinement. Chem. Eng. J. **390**, 124566 (2020). https://doi.org/10.1016/j.cej.2020.124566
21. Z. Yang, F. Gao, H. Du, L. Jin, L. Yan et al., Grain size engineered lead-free ceramics with both large energy storage density and ultrahigh mechanical properties. Nano Energy **58**, 768–777 (2019). https://doi.org/10.1016/j.nanoen.2019.02.003
22. G. Liu, Y. Li, M. Shi, L. Yu, P. Chen et al., An investigation of the dielectric energy storage performance of $Bi(Mg_{2/3}Nb_{1/3})O_3$-modifed $BaTiO_3$ Pb-free bulk ceramics with improved temperature/frequency stability. Ceram. Int. **45**, 19189–19196 (2019). https://doi.org/10.1016/j.ceramint.2019.06.166
23. G. Liu, Y. Li, J. Gao, D. Li, L. Yu et al., Structure evolution, ferroelectric properties, and energy storage performance of $CaSnO_3$ modified $BaTiO_3$-based Pb-free ceramics. J. Alloys Compd. **826**, 154160 (2020). https://doi.org/10.1016/j.jallcom.2020.154160
24. T. Wang, L. Zhang, A. Zhang, J. Liu, L. Kong et al., Synergistic enhanced energy storage performance of NBT-KBT ceramics by $K_{0.5}Na_{0.5}NbO_3$ composition design. J. Alloys Compd. **948**, 169725 (2023). https://doi.org/10.1016/j.jallcom.2023.169725
25. B. Guo, Y. Yan, M. Tang, Z. Wang, Y. Li et al., Energy storage performance of $Na_{0.5}Bi_{0.5}TiO_3$ based lead-free ferroelectric ceramics prepared via non-uniform phase structure modification and rolling process. Chem. Eng. J. **420**, 130475 (2021). https://doi.org/10.1016/j.cej.2021.130475
26. G. Liu, Y. Wang, G. Han, J. Gao, L. Yu et al., Enhanced electrical properties and energy storage performances of NBT-ST Pb-free ceramics through glass modification. J. Alloys Compd. **836**, 154961 (2020). https://doi.org/10.1016/j.jallcom.2020.154961
27. L. Zhang, S. Cao, Y. Li, R. Jing, Q. Hu et al., Achieving ultrahigh energy storage performance over a broad temperature range in $(Bi_{0.5}Na_{0.5})TiO_3$-based eco-friendly relaxor ferroelectric ceramics via multiple engineering processes. J. Alloys Compd. **896**, 163139 (2022). https://doi.org/10.1016/j.jallcom.2021.163139
28. G. Liu, J. Dong, L. Zhang, Y. Yan, R. Jing et al., Phase evolution in $(1–x)(Na_{0.5}Bi_{0.5})TiO_{3–x}SrTiO_3$ solid solutions: a study focusing on dielectric and ferroelectric characteristics. J. Materiomics **6**, 677–691 (2020). https://doi.org/10.1016/j.jmat.2020.05.005
29. S. Wu, B. Fu, J. Zhang, H. Du, Q. Zong et al., Superb energy storage capability for $NaNbO_3$-based ceramics featuring labyrinthine submicro-domains with clustered lattice distortions. Small **19**, e2303915 (2023). https://doi.org/10.1002/smll.202303915
30. H. Wang, S. Wu, B. Fu, J. Zhang, H. Du et al., Hierarchically polar structures induced superb energy storage properties for relaxor $Bi_{0.5}Na_{0.5}TiO_3$-based ceramics. Chem. Eng. J. **471**, 144446 (2023). https://doi.org/10.1016/j.cej.2023.144446
31. T. Karthik, S. Asthana, Enhanced mechanical and ferroelectric properties through grain size refinement in site specific substituted lead free $Na_{0.5–x}K$ x $Bi_{0.5}$ TiO_3 (x = 0–0.10) ceramics. Mater. Lett. **190**, 273–275 (2017). https://doi.org/10.1016/j.matlet.2017.01.025
32. R. Jing, L. Zhang, Q. Hu, D.O. Alikin, V.Y. Shur et al., Phase evolution and relaxor to ferroelectric phase transition boosting ultrahigh electrostrains in $(1–x)(Bi_{1/2}Na_{1/2})TiO_{3-x}(Bi_{1/2}K_{1/2})$ TiO_3 solid solutions. J. Materiomics **8**, 335–346 (2022). https://doi.org/10.1016/j.jmat.2021.09.002
33. C. Wang, X. Yang, Z. Wang, C. He, X. Long, Investigation of switching behavior of acceptor-doped ferroelectric ceramics. Acta Mater. **170**, 100–108 (2019). https://doi.org/10.1016/j.actamat.2019.03.033
34. T. Kainz, M. Naderer, D. Schütz, O. Fruhwirth, F.A. Mautner et al., Solid state synthesis and sintering of solid solutions of BNT–*x*BKT. J. Eur. Ceram. Soc. **34**, 3685–3697 (2014). https://doi.org/10.1016/j.jeurceramsoc.2014.04.040
35. Y. Liu, Y. Li, Z. Zheng, W. Kang, K. Xi et al., Dielectric temperature stability of Nb-modified $Bi_{0.5}(Na_{0.78}K_{0.22})_{0.5}TiO_3$ lead-free ceramics. Ceram. Int. **47**, 4933–4936 (2021). https://doi.org/10.1016/j.ceramint.2020.10.067
36. R.D. Shannon, Revised effective ionic radii and systematic studies of interatomic distances in halides and chalcogenides. Acta Crystallogr. Sect. A **32**, 751–767 (1976). https://doi.org/10.1107/s0567739476001551
37. T. Wang, L. Jin, C. Li, Q. Hu, X. Wei, Relaxor ferroelectric $BaTiO_3$–$Bi(Mg_{2/3}Nb_{1/3})O_3$ ceramics for energy storage application. J. Am. Ceram. Soc. **98**, 559–566 (2015). https://doi.org/10.1111/jace.13325
38. C. Sun, X. Chen, J. Shi, F. Pang, X. Dong et al., Simultaneously with large energy density and high efficiency achieved in $NaNbO_3$-based relaxor ferroelectric ceramics. J. Eur. Ceram. Soc. **41**, 1891–1903 (2021). https://doi.org/10.1016/j.jeurceramsoc.2020.10.049
39. L. Jin, W. Luo, L. Wang, Y. Tian, Q. Hu et al., High thermal stability of electric field-induced strain in $(1–x)(Bi_{0.5}Na_{0.5})$ TiO_3-$xBa_{0.85}Ca_{0.15}Ti_{0.9}Zr_{0.1}O_3$ lead-free ferroelectrics. J. Eur. Ceram. Soc. **39**, 277–286 (2019). https://doi.org/10.1016/j.jeurceramsoc.2018.09.019
40. W. Jo, S. Schaab, E. Sapper, L.A. Schmitt, H.-J. Kleebe et al., On the phase identity and its thermal evolution of lead free

$(Bi_{1/2}Na_{1/2})TiO_3$-6 mol% $BaTiO_3$. J. Appl. Phys. **110**, 074106 (2011). https://doi.org/10.1063/1.3645054

41. Y. Hiruma, Y. Imai, Y. Watanabe, H. Nagata, T. Takenaka, Large electrostrain near the phase transition temperature of $(Bi_{0.5}Na_{0.5})TiO_3$–$SrTiO_3$ ferroelectric ceramics. Appl. Phys. Lett. **92**, 262904 (2008). https://doi.org/10.1063/1.2955533
42. H. Zhang, P. Xu, E. Patterson, J. Zang, S. Jiang et al., Preparation and enhanced electrical properties of grain-oriented $(Bi_{1/2}Na_{1/2})TiO_3$-based lead-free incipient piezoceramics. J. Eur. Ceram. Soc. **35**, 2501–2512 (2015). https://doi.org/10.1016/j.jeurceramsoc.2015.03.012
43. J. Zang, W. Jo, H. Zhang, J. Rödel, $Bi_{1/2}Na_{1/2}TiO_3$–$BaTiO_3$ based thick-film capacitors for high-temperature applications. J. Eur. Ceram. Soc. **34**, 37–43 (2014). https://doi.org/10.1016/j.jeurceramsoc.2013.07.020
44. G. Viola, H. Ning, X. Wei, M. Deluca, A. Adomkevicius et al., Dielectric relaxation, lattice dynamics and polarization mechanisms in $Bi_{0.5}Na_{0.5}TiO_3$-based lead-free ceramics. J. Appl. Phys. **114**, 014107 (2013). https://doi.org/10.1063/1.4812383
45. A.A. Bokov, Z.-G. Ye, Recent progress in relaxor ferroelectrics with perovskite structure. J. Mater. Sci. **41**, 31–52 (2006). https://doi.org/10.1007/s10853-005-5915-7
46. V.V. Shvartsman, D.C. Lupascu, Lead-free relaxor ferroelectrics. J. Am. Ceram. Soc. **95**, 1–26 (2012). https://doi.org/10.1111/j.1551-2916.2011.04952.x
47. T. Wang, J. Hu, H. Yang, L. Jin, X. Wei et al., Dielectric relaxation and Maxwell-Wagner interface polarization in Nb_2O_5 doped $06.5BiFeO_3$–$0.35BaTiO_3$ ceramics. J. Appl. Phys. **121**, 084103 (2017). https://doi.org/10.1063/1.4977107
48. L.E. Cross, Relaxor ferroelectrics. Ferroelectrics **76**, 241–267 (1987). https://doi.org/10.1080/00150198708016945
49. H. Pan, S. Lan, S. Xu, Q. Zhang, H. Yao et al., Ultrahigh energy storage in superparaelectric relaxor ferroelectrics. Science **374**, 100–104 (2021). https://doi.org/10.1126/science.abi7687
50. H. Pan, F. Li, Y. Liu, Q. Zhang, M. Wang et al., Ultrahigh-energy density lead-free dielectric films via polymorphic nanodomain design. Science **365**, 578–582 (2019). https://doi.org/10.1126/science.aaw8109
51. C. Zhu, Z. Cai, B. Luo, L. Guo, L. Li et al., High temperature lead-free BNT-based ceramics with stable energy storage and dielectric properties. J. Mater. Chem. A **8**, 683–692 (2020). https://doi.org/10.1039/c9ta10347c
52. L. Zhang, R. Jing, Y. Huang, Q. Hu, D.O. Alikin et al., Ultrahigh electrostrictive effect in potassium sodium niobate-based lead-free ceramics. J. Eur. Ceram. Soc. **42**, 944–953 (2022). https://doi.org/10.1016/j.jeurceramsoc.2021.11.037
53. W. Wang, L. Zhang, W. Shi, Y. Yang, D. Alikin et al., Enhanced energy storage properties in lead-free $(Na_{0.5}Bi_{0.5})_{0.7}Sr_{0.3}TiO_3$-based relaxor ferroelectric ceramics through a cooperative optimization strategy. ACS Appl. Mater. Interfaces **15**, 6990–7001 (2023). https://doi.org/10.1021/acsami.2c21969
54. W. Wang, L. Zhang, Y. Yang, W. Shi, Y. Huang et al., Enhancing energy storage performance in $Na_{0.5}Bi_{0.5}TiO_3$-based lead-free relaxor ferroelectric ceramics along a stepwise optimization route. J. Mater. Chem. A **11**, 2641–2651 (2023). https://doi.org/10.1039/D2TA09395B
55. W. Jo, T. Granzow, E. Aulbach, J. Rödel, D. Damjanovic, Origin of the large strain response in $(K_{0.5}Na_{0.5})NbO_3$-modified $(Bi_{0.5}Na_{0.5})TiO_3$–$BaTiO_3$ lead-free piezoceramics. J. Appl. Phys. **105**, 094102 (2009). https://doi.org/10.1063/1.3121203
56. G. Viola, Y. Tian, C. Yu, Y. Tan, V. Koval et al., Electric field-induced transformations in bismuth sodium titanate-based materials. Prog. Mater. Sci. **122**, 100837 (2021). https://doi.org/10.1016/j.pmatsci.2021.100837
57. W. Shi, L. Zhang, R. Jing, Q. Hu, X. Zeng et al., Relaxor antiferroelectric-like characteristic boosting enhanced energy storage performance in eco-friendly $(Bi_{0.5}Na_{0.5})TiO_3$-based ceramics. J. Eur. Ceram. Soc. **42**, 4528–4538 (2022). https://doi.org/10.1016/j.jeurceramsoc.2022.04.057
58. N. Luo, K. Han, M.J. Cabral, X. Liao, S. Zhang et al., Constructing phase boundary in $AgNbO_3$ antiferroelectrics: pathway simultaneously achieving high energy density and efficiency. Nat. Commun. **11**, 4824 (2020). https://doi.org/10.1038/s41467-020-18665-5
59. A. Xie, R. Zuo, Z. Qiao, Z. Fu, T. Hu et al., $NaNbO_3$-$(Bi_{0.5}Li_{0.5})TiO_3$ lead-free relaxor ferroelectric capacitors with superior energy-storage performances via multiple synergistic design. Adv. Energy Mater. **11**, 2101378 (2021). https://doi.org/10.1002/aenm.202101378
60. J. Jiang, X. Meng, L. Li, S. Guo, M. Huang et al., Ultrahigh energy storage density in lead-free relaxor antiferroelectric ceramics via domain engineering. Energy Storage Mater. **43**, 383–390 (2021). https://doi.org/10.1016/j.ensm.2021.09.018
61. Q. Hu, X. Wei, Abnormal phase transition and polarization mismatch phenomena in $BaTiO_3$-based relaxor ferroelectrics. J. Adv. Dielect. **9**, 1930002 (2019). https://doi.org/10.1142/s2010135x19300020
62. F. Yan, K. Huang, T. Jiang, X. Zhou, Y. Shi et al., Significantly enhanced energy storage density and efficiency of BNT-based perovskite ceramics via A-site defect engineering. Energy Storage Mater. **30**, 392–400 (2020). https://doi.org/10.1016/j.ensm.2020.05.026
63. X. Zhao, W. Bai, Y. Ding, L. Wang, S. Wu et al., Tailoring high energy density with superior stability under low electric field in novel $(Bi_{0.5}Na_{0.5})TiO_3$-based relaxor ferroelectric ceramics. J. Eur. Ceram. Soc. **40**, 4475–4486 (2020). https://doi.org/10.1016/j.jeurceramsoc.2020.05.078
64. D. Li, Y. Lin, Q. Yuan, M. Zhang, L. Ma et al., A novel lead-free $Na_{0.5}Bi_{0.5}TiO_3$-based ceramic with superior comprehensive energy storage and discharge properties for dielectric capacitor applications. J. Materiomics **6**, 743–750 (2020). https://doi.org/10.1016/j.jmat.2020.06.005
65. H. Qi, R. Zuo, Linear-like lead-free relaxor antiferroelectric $(Bi_{0.5}Na_{0.5})TiO_3$–$NaNbO_3$ with giant energy-storage density/efficiency and super stability against temperature and frequency. J. Mater. Chem. A **7**, 3971–3978 (2019). https://doi.org/10.1039/C8TA12232F
66. H. Yang, F. Yan, Y. Lin, T. Wang, Novel strontium titanate-based lead-free ceramics for high-energy storage

 https://doi.org/10.1007/s40820-023-01290-4

applications. ACS Sustain. Chem. Eng. **5**, 10215–10222 (2017). https://doi.org/10.1021/acssuschemeng.7b02203

67. Y. Huang, L. Zhang, R. Jing, Q. Hu, D.O. Alikin et al., Thermal stability of dielectric and energy storage performances of Ca-substituted BNTZ ferroelectric ceramics. Ceram. Int. **47**, 6298–6309 (2021). https://doi.org/10.1016/j.ceramint.2020.10.208
68. G. Liu, J. Dong, L. Zhang, L. Yu, F. Wei et al., $Na_{0.25}Sr_{0.5}Bi_{0.25}TiO_3$ relaxor ferroelectric ceramic with greatly enhanced electric storage property by a B-site ion doping. Ceram. Int. **46**, 11680–11688 (2020). https://doi.org/10.1016/j.ceramint.2020.01.199
69. R. Kang, Z. Wang, X. Lou, W. Liu, P. Shi et al., Energy storage performance of $Bi_{0.5}Na_{0.5}TiO_3$-based relaxor ferroelectric ceramics with superior temperature stability under low electric fields. Chem. Eng. J. **410**, 128376 (2021). https://doi.org/10.1016/j.cej.2020.128376
70. G. Liu, L. Hu, Y. Wang, Z. Wang, L. Yu et al., Investigation of electrical and electric energy storage properties of La-doped $Na_{0.3}$ $Sr_{0.4}Bi_{0.3}TiO_3$ based Pb-free ceramics. Ceram. Int. **46**, 19375–19384 (2020). https://doi.org/10.1016/j.ceramint.2020.04.280
71. L. Yu, J. Dong, M. Tang, Y. Liu, F. Wu et al., Enhanced electrical energy storage performance of Pb-free A-site La^{3+}-doped $0.85Na_{0.5}Bi_{0.5}TiO_3$–$0.15CaTiO_3$ ceramics. Ceram. Int. **46**, 28173–28182 (2020). https://doi.org/10.1016/j.ceramint.2020.07.316
72. X. Zhang, D. Hu, Z. Pan, X. Lv, Z. He et al., Enhancement of recoverable energy density and efficiency of lead-free relaxor-ferroelectric BNT-based ceramics. Chem. Eng. J. **406**, 126818 (2021). https://doi.org/10.1016/j.cej.2020.126818
73. X. Qiao, F. Zhang, D. Wu, B. Chen, X. Zhao et al., Superior comprehensive energy storage properties in $Bi_{0.5}Na_{0.5}TiO_3$-based relaxor ferroelectric ceramics. Chem. Eng. J. **388**, 124158 (2020). https://doi.org/10.1016/j.cej.2020.124158
74. F. Yan, X. Zhou, X. He, H. Bai, S. Wu et al., Superior energy storage properties and excellent stability achieved in environment-friendly ferroelectrics via composition design strategy. Nano Energy **75**, 105012 (2020). https://doi.org/10.1016/j.nanoen.2020.105012
75. D. Hu, Z. Pan, X. Zhang, H. Ye, Z. He et al., Greatly enhanced discharge energy density and efficiency of novel relaxation ferroelectric BNT–BKT-based ceramics. J. Mater. Chem. C **8**, 591–601 (2020). https://doi.org/10.1039/C9TC05528B
76. L. Yang, X. Kong, Z. Cheng, S. Zhang, Ultra-high energy storage performance with mitigated polarization saturation in lead-free relaxors. J. Mater. Chem. A **7**, 8573–8580 (2019). https://doi.org/10.1039/c9ta01165j
77. T. Li, P. Chen, F. Li, C. Wang, Energy storage performance of $Na_{0.5}Bi_{0.5}TiO_3$-$SrTiO_3$ lead-free relaxors modified by $AgNb_{0.85}Ta_{0.15}O_3$. Chem. Eng. J. **406**, 127151 (2021). https://doi.org/10.1016/j.cej.2020.127151
78. Z. Jiang, H. Yang, L. Cao, Z. Yang, Y. Yuan et al., Enhanced breakdown strength and energy storage density of lead-free Bi05Na05TiO3-based ceramic by reducing the oxygen vacancy concentration. Chem. Eng. J. **414**, 128921 (2021). https://doi.org/10.1016/j.cej.2021.128921
79. Z. Yang, H. Du, L. Jin, Q. Hu, H. Wang et al., Realizing high comprehensive energy storage performance in lead-free bulk ceramics *via* designing an unmatched temperature range. J. Mater. Chem. A **7**, 27256–27266 (2019). https://doi.org/10.1039/C9TA11314B
80. G. Zhang, P. Liu, B. Fan, H. Liu, Y. Zeng et al., Large energy density in Ba doped $Pb_{0.97}La_{0.02}(Zr_{0.65}Sn_{0.3}Ti_{0.05})O_3$ antiferroelectric ceramics with improved temperature stability. IEEE Trans. Dielectr. Electr. Insul. **24**, 744–748 (2017). https://doi.org/10.1109/TDEI.2017.006161
81. L. Jin, W. Luo, L. Hou, Y. Tian, Q. Hu et al., High electric field-induced strain with ultra-low hysteresis and giant electrostrictive coefficient in Barium strontium titanate lead-free ferroelectrics. J. Eur. Ceram. Soc. **39**, 295–304 (2019). https://doi.org/10.1016/j.jeurceramsoc.2018.09.005
82. H. Ye, F. Yang, Z. Pan, D. Hu, X. Lv et al., Significantly improvement of comprehensive energy storage performances with lead-free relaxor ferroelectric ceramics for high-temperature capacitors applications. Acta Mater. **203**, 116484 (2021). https://doi.org/10.1016/j.actamat.2020.116484
83. A.K. Yadav, H. Fan, B. Yan, C. Wang, J. Ma et al., Enhanced storage energy density and fatigue free properties for $0.94Bi_{0.50}(Na_{0.78}K_{0.22})_{0.50}Ti_{1-x}(Al_{0.50}Nb_{0.50})xO_3$–$_{0.06}BaZrO_3$ ceramics. Ceram. Int. **46**, 17044–17052 (2020). https://doi.org/10.1016/j.ceramint.2020.03.292
84. A. Xie, H. Qi, R. Zuo, Achieving remarkable amplification of energy-storage density in two-step sintered $NaNbO_3$–$SrTiO_3$ antiferroelectric capacitors through dual adjustment of local heterogeneity and grain scale. ACS Appl. Mater. Interfaces **12**, 19467–19475 (2020). https://doi.org/10.1021/acsami.0c00831